

Perforation of 5083-H116 Aluminum Armor Plates with Ogive-Nose Rods and 7.62 mm APM2 Bullets

T. Børvik · M.J. Forrestal · T.L. Warren

Received: 16 February 2009 / Accepted: 5 June 2009 / Published online: 25 June 2009
© Society for Experimental Mechanics 2009

Abstract We conducted an experimental and analytical study to understand the mechanisms and dominant parameters for ogive-nose rods and 7.62 mm APM2 bullets that perforate 5083-H116 aluminum armor plates. The 20-mm-diameter, 95-mm-long, ogive-nose, 197 g, hard steel rods were launched with a gas gun to striking velocities between 230–370 m/s. The 7.62-mm-diameter, 10.7 g, APM2 bullet consists of a brass jacket, lead filler, and a 5.25 g, ogive-nose, hard steel core. The brass and lead were stripped from the APM2 bullets by the targets, so we conducted ballistic experiments with both the APM2 bullets and only the hard steel cores. These projectiles were fired from a rifle to striking velocities between 480–950 m/s. Targets were 20, 40, and 60-mm-thick, where the 40 and 60-mm-thick targets were made up of layered 20-mm-thick plates in

contact with each other. The measured ballistic-limit velocities for the APM2 bullets were 4, 6, and 12% smaller than that for the hard steel cores for the 20, 40, and 60-mm-thick targets, respectively. Thus, the brass jacket and lead filler had a relatively small effect on the perforation process. In addition, we conducted large strain, compression tests on the 5083-H116 aluminum plate material for input to perforation equations derived from a cavity-expansion model for the ogive-nose rods and steel core projectiles. Predictions for the rod and hard steel core projectiles are shown to be in good agreement with measured ballistic-limit and residual velocity data. These experimental results and perforation equations display the dominant problem parameters.

Keywords Aluminum armor plates · Ogive-nose rods · 7.62 mm APM2 bullets · Experimental study · Perforation equations

T. Børvik (✉)
Structural Impact Laboratory (SIMLab),
Centre for Research-based Innovation (CRI),
Department of Structural Engineering,
Norwegian University of Science and Technology,
NO-7491 Trondheim, Norway
e-mail: tore.borvik@ntnu.no

T. Børvik
Norwegian Defence Estates Agency,
Research and Development Department,
NO-0015 Oslo, Norway

M.J. Forrestal (SEM member)
1805 Newton Pl, NE,
Albuquerque, NM 87106, USA
e-mail: mmforrestal@comcast.net

T.L. Warren
3804 Shenandoah Pl, NE,
Albuquerque, NM 87111, USA
e-mail: tlwarre@msn.com

Introduction

For this paper, we study the perforation of 5083-H116 aluminum armor plates with ogive-nose, rigid rod projectiles and 7.62 mm APM2 bullets. Recent related work on rigid rods is given by Forrestal and Warren [1], who present closed-form perforation equations for rigid, conical and ogival nose, rod projectiles that perforate 6061-T651 and 5083-H131 aluminum armor plates. In addition, Børvik et al. [2] present finite-element calculations for rigid, conical nose rods that perforate 5083-H116 aluminum armor plates. Both of these studies compare predictions with many sets of perforation data. Dey et al. [3] present experimental results and finite-element calculations for the perforation of steel plates with blunt and ogive-nose projectiles.



The major focus of this study is on 7.62 mm APM2 bullets. We conducted perforation experiments with the full 10.7 g, APM2 bullets and only the 5.25 g, hard steel cores from the full bullet. Our data shows the perforation process is dominated by the hard steel core. Predictions from our analytical model [1] are in good agreement with the hard steel core data, so these closed-form perforation equations are able to show the relevant problem parameters. In other papers concerned with 7.62 APM2 bullets, Gooch et al. [4] present ballistic-limit data for 6061-T651 aluminum plates. In addition, Anderson [5] present computer modeling and data for ceramic tiles, and Børvik et al. [6] present finite-element simulations and data for high-strength steel plates.

In the next sections, we describe the targets and projectiles, describe the experimental procedures, present the perforation data, and compare predictions and measurements. A summary of perforation equations from previously published models used for ballistic-limit and residual velocity predictions is presented in the [Appendix](#).

Projectiles

Ogive-Nose Rod Projectile

Figure 1(a) shows the dimensions of the 3.0 caliber-radius-head (CRH=3.0), ogive-nose projectile. This projectile has shank length $L=62$ mm, nose length $l=33$ mm, and diameter $2a=20$ mm. The steel projectile has density $\rho_p=7850$ kg/m³, mass $m=0.197$ kg, and hardness R_c 53. More material data is given in [7, 8]. From [1], the projectile mass is given by

$$m = \pi \rho_p a^2 (L + k_1 l) \quad (1a)$$

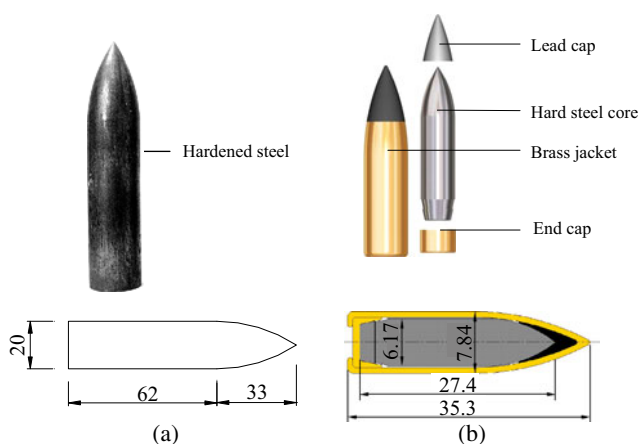


Fig. 1 Geometry and dimensions (in mm) of a) 20 mm ogive-nose hardened steel projectile and b) 7.62 mm APM2 bullet (Note: not in scale)

$$k_1 = (4\psi^2 - 4\psi/3 + 1/3) - \frac{4\psi^2(2\psi - 1)}{\sqrt{4\psi - 1}} \sin^{-1} \left[\frac{\sqrt{4\psi - 1}}{2\psi} \right] \quad (1b)$$

$$\psi = \frac{1}{4} \left[\left(\frac{l}{a} \right)^2 + 1 \right] \quad (1c)$$

where ψ is the caliber-radius-head (CRH) for the ogive nose.

The 7.62 mm APM2 Bullet

Figure 1(b) shows the dimensions and the parts that make up the APM2 bullet. The 7.62 mm-diameter, 10.7 g, APM2 bullet consists of a brass jacket, an end cap, lead filler, and a 5.25 g, ogive-nose, hard steel core. The steel core has hardness R_c 63 and CRH=3.0 ($\psi=3.0$). More details for the APM2 bullet not needed for this study can be found in [5, 6].

The Hard Steel Core Projectile

As previously mentioned, we will present data and predictions for the hard steel core projectile. Our perforation model [1] is for a rigid, ogive-nose, rod projectile. Note that the shank of the steel core of the 7.62 mm APM2 bullet shown in Fig. 1(b) is truncated towards the end cap, so we find an equivalent shank length L from equations (1a–c) that matches the measured mass of the steel core. With mass $m=5.25$ g, diameter $2a=6.17$ mm, and $\psi=3.0$, we find the nose length $l=10.2$ mm and shank length $L=16.8$ mm.

AA5083-H116 Target Plates

Material Description and Specifications

Wrought aluminum alloys are divided into seven major classes that are designated by their principle alloying elements [9]. The class AA5xxx consists of aluminum-magnesium elements and is well suited for rolling, so plates are an important product. The major use of AA5xxx plates is for naval structures that include ship hulls and offshore topsides. These plates are also used for ballistic protection [2, 4]. For this study, the aluminum alloy AA5083-H116 was chosen due to its high strength. Many more details about AA5083-H116 are reported in [10–12]. We also point out that due to the manufacturing process, the yield strength can vary with plate thickness for this alloy. For this study, all targets came from 20-mm-thick plates.

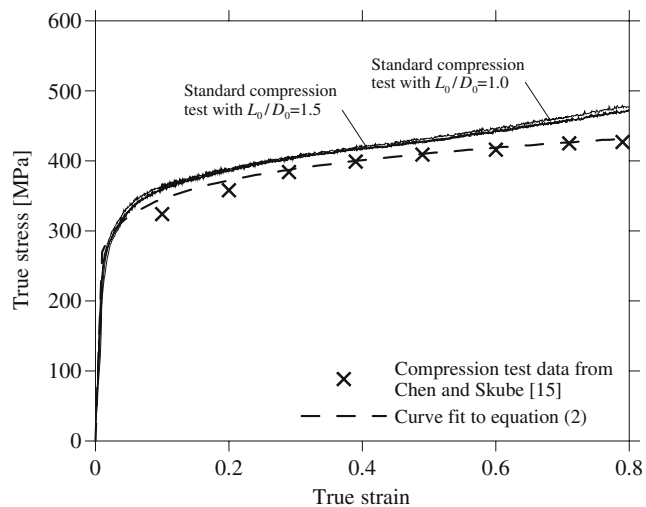


Fig. 2 Typical true stress-strain curves from compression tests of cylindrical specimens with $L_0/D_0=1.0$ and 1.5 taken in the thickness direction of a 20-mm-thick plate compared to data from compression tests from Chen and Skube [15]. A curve fit to the data from Chen and Skube (with $E=71$ GPa, $Y=240$ MPa, and $n=0.108$) is also shown

The US Army Research Laboratory [12] specifies some minimum mechanical properties for aluminum alloy, armor plates. For AA5083-H116 plates, the minimum suggested mechanical properties include: ultimate tensile strength $\sigma_u=283$ MPa, yield strength defined by the 0.2% offset $\sigma_0=200$ MPa, and percent elongation at tensile failure $\varepsilon_f=0.10$. In addition, the ASM Metals Handbook [13] suggested properties are $\sigma_u=315$ MPa and $\sigma_0=230$ MPa. We obtained 20-mm-thick, 5083-H116, target plates from Alcoa Europe.

The supplier provided inspection certification sheets with tensile data from four tests. Data include $\sigma_u=325$ MPa, $\sigma_0=244$ MPa, $\varepsilon_f=0.16$; $\sigma_u=323$ MPa, $\sigma_0=244$ MPa, $\varepsilon_f=0.16$; $\sigma_u=318$ MPa, $\sigma_0=246$ MPa, $\varepsilon_f=0.16$; $\sigma_u=317$ MPa, $\sigma_0=238$ MPa, $\varepsilon_f=0.16$. Therefore, tensile data from the Alcoa Europe, inspection certification sheets meet the US Army Research Laboratory [12] minimum requirements and are in close agreement with the ASM Metals Handbook [13] suggested properties.

Compression Stress-Strain Experiments

We later show that the ogive nose compresses the material in the plane of the plate and opens a hole with nearly the diameter of the shank. This deformation mechanism, called ductile hole growth, is a basic assumption for our cavity-expansion, perforation model [1]. Compression stress-strain data are required input to these perforation equations. First, we conducted standard compression tests with cylindrical specimens. Next, we conducted compression tests to true strains of 0.80 with the technique described by Kawahara [14] and Chen and Skube [15].

Standard uniaxial compression or upsetting tests in the thickness direction of the 20-mm-thick plates were conducted using cylindrical specimens with an initial diameter $D_0=10$ mm, and an initial length $L_0=10$ mm and 15 mm ($L_0/D_0=1.0$ and 1.5). After grinding the end surfaces, the specimens were precisely aligned between two hard, polished anvils in a servo-hydraulic test machine to obtain a homogenous deformation of the specimen. To minimize

Table 1 Test data

Test nr.	20mm projectiles		APM2 bullets		APM2 bullet - core only		APM2 bullet		APM2 bullet - core only		APM2 bullet		APM2 bullet - core only	
	20mm targets		20mm targets		20mm targets		2×20 mm targets		2×20 mm targets		3×20 mm targets		3×20 mm targets	
	V_5 [m/s]	V_r [m/s]	V_5 [m/s]	V_r [m/s]	V_5 [m/s]	V_r [m/s]	V_5 [m/s]	V_r [m/s]	V_5 [m/s]	V_r [m/s]	V_5 [m/s]	V_r [m/s]	V_5 [m/s]	V_r [m/s]
1	360.3	281.3	822.4	694.3	741.4	532.2	866.3	486.2	741.3	0	925.1	77.9	1014.6	0
2	248.2	51.6	715.1	551.6	614.1	350.9	802.2	378.8	802.6	218.8	905.6	0	1092.7	521.9
3	242.1	0	614.9	393.7	545.5	189.2	669.8	0	901.3	462.2	928.8	150.0	1079.1	487.6
4	247.7	50.6	562.2	300.6	552.3	221.5	700.6	0	800.1	161.7	914.5	0	1044.0	403.0
5	293.4	173.7	524.8	201.1	532.4	169.7	771.8	310.6	787.3	200.2	912.9	85.4	1032.8	376.8
6	271.2	133.1	497.7	34.4	509.5	0	742.4	129.1	763.8	0	944.8	208.5	1059.1	399.7
7			480.0	0	517.6	44.8	715.5	0	761.7	0	955.7	255.4	1029.3	350.7
8			497.9	85.3	854.1	700.4	728.1	75.9	751.4	0	933.6	167.0	1007.6	0
9			491.9	0	500.9	0	747.9	211.8	780.5	0			1023.5	0
10					668.1	428.6	914.5	603.7	784.4	201.9			1027.8	376.4
11									995.3	640.9			651.4	0
12									867.6	402.4				

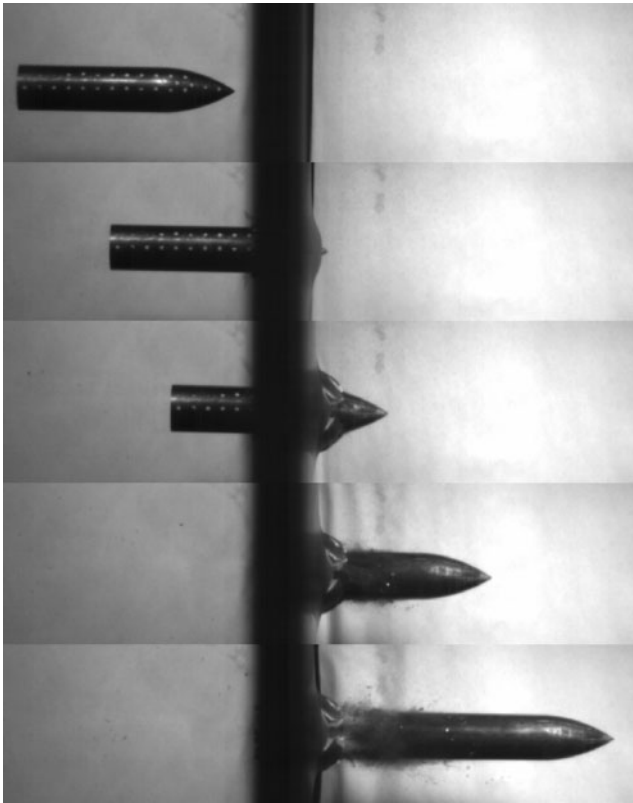


Fig. 3 High-speed video images showing the perforation process of a monolithic 20-mm-thick AA5083-H116 plate impacted by a 20 mm ogive-nose projectile ($V_s=271$ m/s, $V_r=133$ m/s)

the effect of barreling caused by friction between the specimen surfaces and the anvils, a graphite paste was used to lubricate the interface. The tests were conducted at room temperature with a constant strain rate of about 10^{-3}s^{-1} . The force was measured by a calibrated load cell, and the displacement was measured by the actuator stroke and an extensometer attached to the anvils. Based on these measurements, stresses and strains were calculated. Typical true stress-strain curves from the standard compression tests are given in Fig. 2. Note that the compression test data with $L_0/D_0=1.0$ and 1.5 are in close agreement to a true strain of at least 0.4.

Chen and Skube [15] provided the authors with compression stress-strain data to true strains of 0.80. To obtain these large compression strains without barreling, a special sample design must be used [14, 15]. For these material experiments, the samples had initial length $L_0=10.16$ mm and initial diameter $D_0=7.62$ mm ($L_0/D_0=1.33$). Then, three concentric grooves were machined into the top and bottom of the samples to retain lubrication during the compression tests. These grooves were semi-circular in shape with radius 0.254 mm. The lubrication was molybdenum disulfide. Grid lines were put on the samples that were photographed during compression at a strain rate of about 10^{-3}s^{-1} . The samples were precisely aligned between

two polished anvils in a servo-hydraulic test machine, and force was measured by a calibrated load cell. The samples showed negligible barreling. Based on the force and deformation measurements, stresses and strains were calculated. Data from a typical experiment along with data from the conventional compression tests are shown in Fig. 2.

For input to our cavity-expansion perforation model, the uniaxial compression data were curve-fit with

$$\sigma = \begin{cases} E\varepsilon & , \quad \sigma < Y \\ Y\left(\frac{E\varepsilon}{Y}\right)^n & , \quad \sigma \geq Y \end{cases} \quad (2a, b)$$

where σ is true stress, ε is true strain, E is Young's modulus, Y is the yield stress, and n is the strain-hardening exponent. Figure 2 shows this power-law data fit from equations (2a,b) with $E=71$ GPa, $Y=240$ MPa, and $n=0.108$.



(a) Test # 5 ($V_s = 293.4\text{m/s}$, $V_r = 173.7\text{m/s}$)



(b) Test # 4 ($V_s = 247.7\text{m/s}$, $V_r = 50.6\text{m/s}$)



(c) Test # 3 ($V_s = 242.1\text{m/s}$, $V_r = 0\text{m/s}$)

Fig. 4 Pictures of cross-sections of 20-mm-thick monolithic AA5083-H116 targets perforated by a 20 mm ogive-nose projectile. (a) Test # 5 ($V_s=293.4$ m/s, $V_r=173.7$ m/s), (b) Test # 4 ($V_s=247.7$ m/s, $V_r=50.6$ m/s), (c) Test # 3 ($V_s=242.1$ m/s, $V_r=0$ m/s)

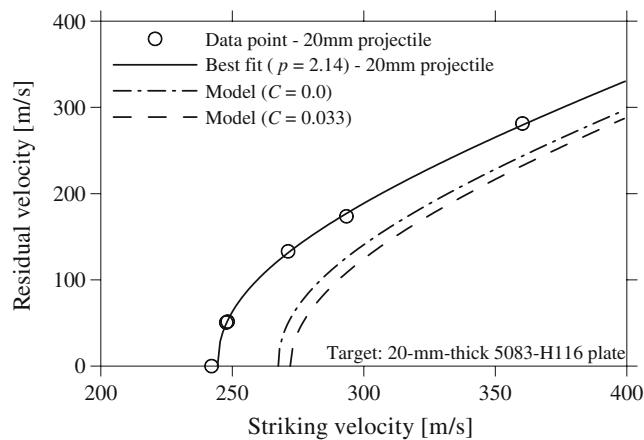


Fig. 5 Comparison of measured and predicted striking versus residual velocity curves for a 20 mm ogive-nose rod projectiles and a 20-mm-thick monolithic AA5083-H116 target plate

Ogive-Nose Rod Experiments

The ballistic tests were carried out in a compressed gas-gun facility described in detail by Børvik et al. [8]. Projectiles, shown in Fig. 1(a), were mounted in a nine piece, serrated sabot that was stripped by a sabot trap prior to impact. Square plates with length 600 mm and thickness 20 mm were clamped into a circular frame with diameter 500 mm and tightened with 16 bolts. Striking and residual velocities were measured with laser optical devices that were shown to be accurate to within 1–2% [6]. In addition, the overall perforation process was photographed with a high-speed video camera. More details on the experimental arrangement and instrumentation are discussed in [3, 6, 8].

We conducted six experiments and present the striking velocities V_s and residual velocities V_r in Table 1. Figure 3 shows some high-speed photographs of the overall perforation process, and Fig. 4 shows some post-test photographs of the 20-mm-thick plates. The last frame in Fig. 3 shows the projectile exiting the target plate and proves that most of the deformed plate material is pushed in the plane of the plate. Figure 4 shows that the holes had nearly the projectile shank diameter. Thus, we observe the ductile, hole-growth, deformation process that guided the cavity-expansion assumption.

The perforation equations from our cavity-expansion model and the data-fit equations are presented in the

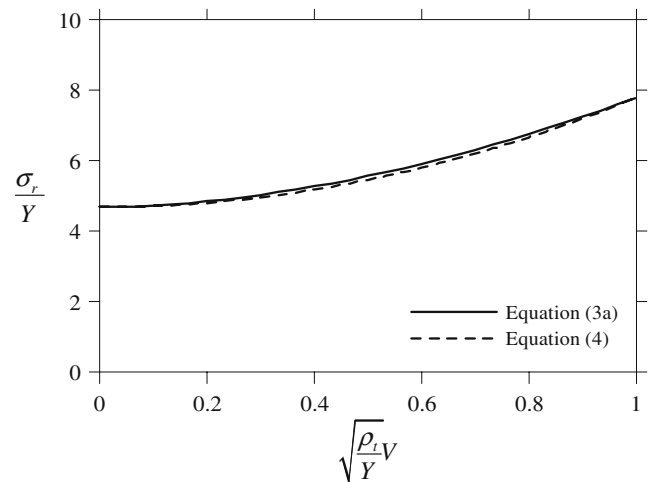


Fig. 6 Dimensionless radial stress at the cavity surface versus dimensionless cavity-expansion velocity for 5083-H116 aluminum with $E=71$ GPa, $Y=240$ MPa, $\nu=0.33$, $n=0.108$, $\rho_t=2660$ kg/m³, $\sigma_5=1.12$ GPa, $B_0=3.105$ and $I=4.09$

Appendix. Figure 5 gives a least-squares curve-fit to the data from equation (10) with $p=2.14$ and a prediction from our cavity-expansion, perforation model. For the data-fit, we used the five data points above the ballistic-limit velocity to obtain the ballistic-limit velocity of $V_{bl}=244$ m/s given in Table 2. The model predictions used the material parameters given in Fig. 6 and equations (5–8). We present predictions with $C=0$ and $C=0.031$. As discussed in the **Appendix**, the $C=0$ prediction neglects radial plate inertia. For $C=0$, we predict $V_{bl}=267$ m/s, and for $C=0.031$ we predict $V_{bl}=272$ m/s. Note that the effect of radial inertia is very small for this problem. The model predicts a V_{bl} about 10% larger than the measured value, but we consider this to be reasonably good agreement for these closed-form, perforation equations. Thus, equations (5, 6) with $C=0$ show the dominant problem parameters.

The 7.62 mm APM2 Bullet and Hard Steel Core Experiments

A 7.62-mm-diameter, 63-mm-long, smooth-bore Mauser gun that used adjusted ammunition fired these projectiles. The APM2 bullets fit the gun bore, and the 6.17-mm-diameter

Table 2 Experimentally obtained ballistic-limit velocities for various projectile and target configurations

Projectile type	AA5083-H116 target plate		
	1×20 mm [m/s]	2×20 mm [m/s]	3×20 mm [m/s]
Ogive-nose steel	244	Not available	Not available
APM2 bullet	492	722	912
APM2 core only	513	767	1025

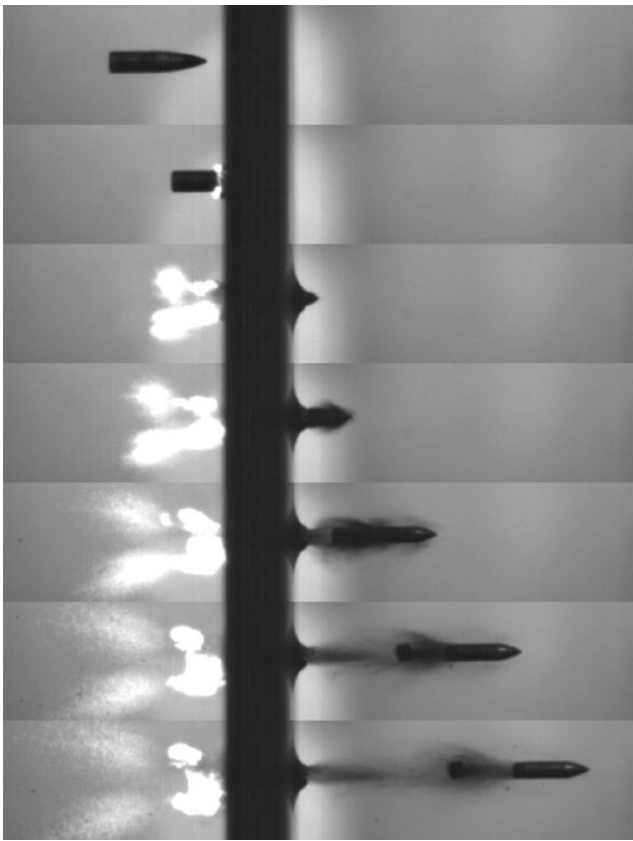


Fig. 7 High-speed video images showing the perforation process of a monolithic 20-mm-thick AA5083-H116 plate impacted by an APM2 bullet ($V_s=562.2$ m/s, $V_r=300.6$ m/s)

cores were encased in a 7.62-mm-diameter, 0.3 g plastic sabot. For these tests, the Mauser gun stock was removed and the rifle was mounted in a rigid rack inside the chamber of the gas-gun [8]. Square target plate configurations with a length of 300 mm and thicknesses of 1×20 mm, 2×20 mm, and 3×20 mm were firmly clamped to a frame by two beams. This provided a fixed boundary for the horizontal sides of the targets, and the vertical sides remained free. The in-plane distance between each shot and the target boundary was 100 mm, and a maximum of four shots were allowed in each target before it was replaced. All layered plates were in direct contact with each other, so plate spacing was not considered in this study. Both the experimental procedures and measurements used in these tests were similar to those described in the previous section for the ogive-nose rod experiments.

We conducted a large number of tests with these projectiles and three plate thickness configurations. The ammunition was adjusted so that the projectiles impacted the targets at striking velocities just below and well above the ballistic-limit velocities. The measured data for the tests are given in Table 1 and Table 2. Figure 7 shows typical, high-speed video images of the perforation process for a 20-mm-thick plate impacted by the APM2 bullet. Note that the brass jacket and

lead cap are completely stripped from the hard core by the target. Figure 8 shows some high-speed video images of the perforation process for a 20-mm-thick plate impacted by the hard steel core. Figure 9 shows pictures of some cross-sections of the three target plate configurations.

The most important results of our study are shown in Fig. 10 that display the residual velocity versus striking velocity curves. Data for the APM2 bullets and hard cores were curve-fit to the data with the least squares method and equation (10). The largest differences shown in Fig. 10 between the results of the two projectiles occur at and near the ballistic-limit velocities that are recorded in Table 2. The measured ballistic-limit velocities for the APM2 bullets were 4, 6, and 12% smaller than that for the hard steel cores for the 1×20 mm, 2×20 mm, and 3×20 mm plate configurations, respectively. Thus, the brass jacket and lead filler had a relatively small effect on the perforation process even though the masses of the APM2 bullet and hard steel core are 10.7 g and 5.25 g, respectively.

Figure 11 compares the cavity-expansion, model predictions discussed in the Appendix and data for the hard steel core projectile. Predictions used the material param-

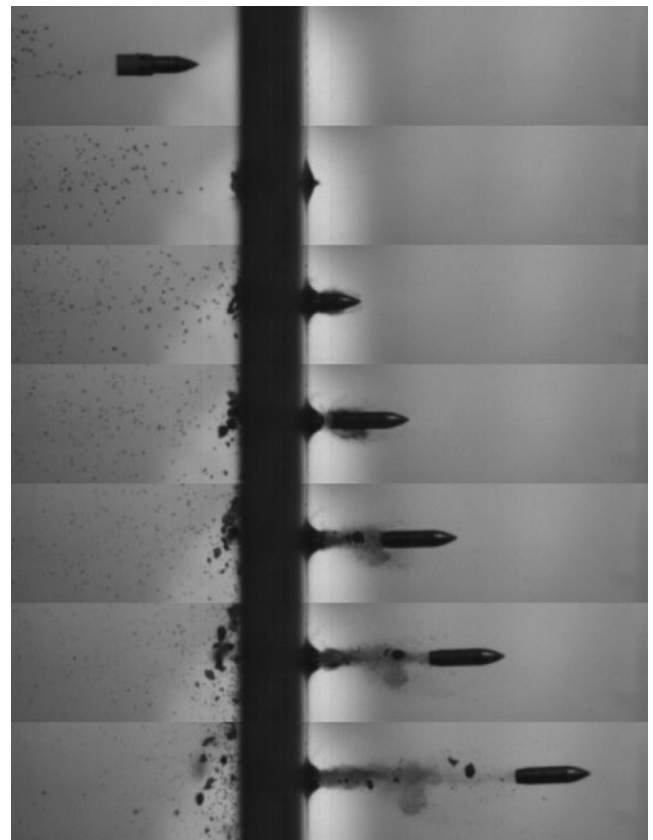
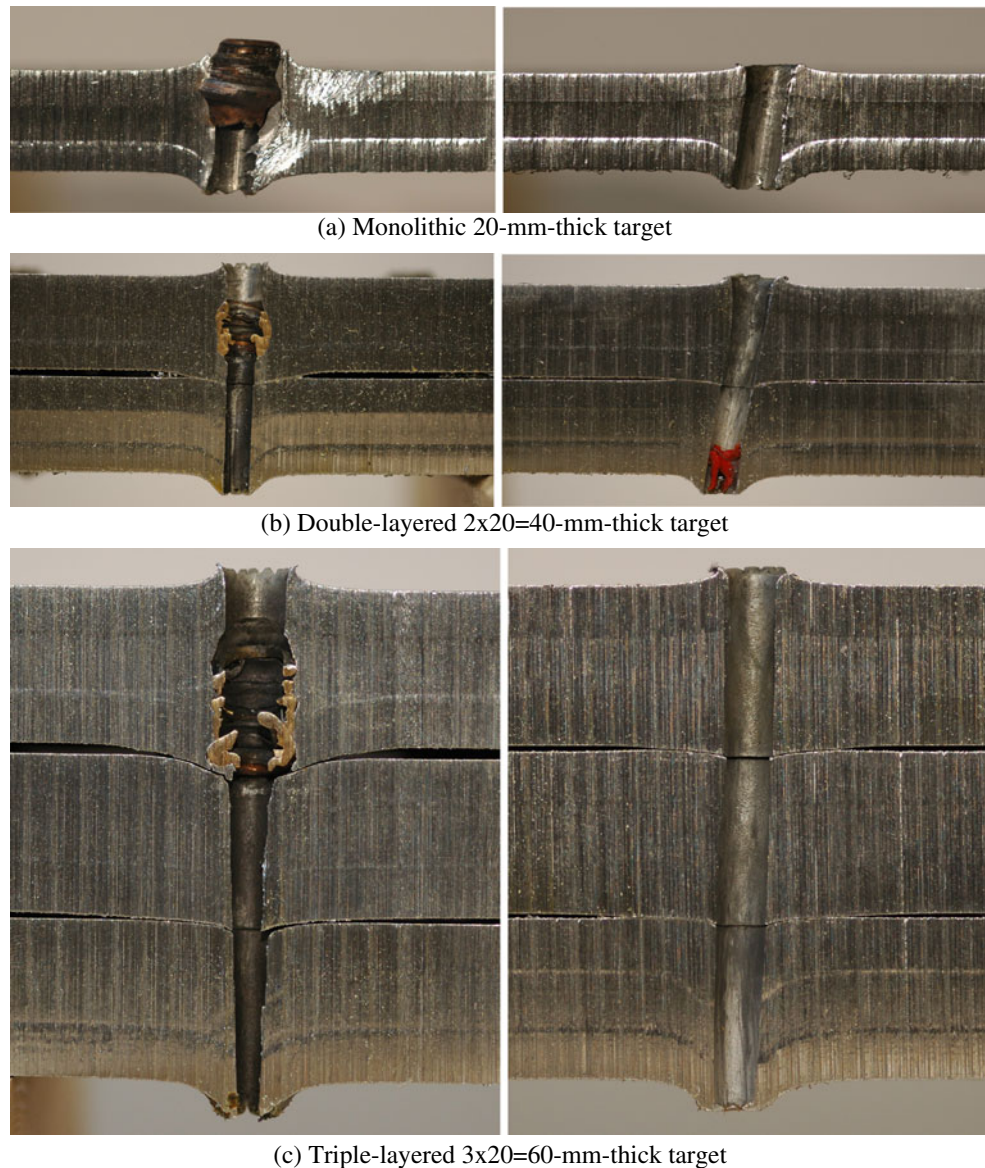


Fig. 8 High-speed video images showing the perforation process of a monolithic 20-mm-thick AA5083-H116 plate impacted by only the hard core of the APM2 bullet mounted in a sabot ($V_s=532.4$ m/s, $V_r=169.7$ m/s)

Fig. 9 Pictures of cross-section of monolithic, double-layered and triple-layered target plates perforated by 7.62 mm APM2 bullets (left) and sabot-mounted hard cores only (right). **(a)** Monolithic 20-mm-thick target, **(b)** Double-layered $2 \times 20=40$ -mm-thick target, **(c)** Triple-layered $3 \times 20=60$ -mm-thick target



eters given in Fig. 6 and equations (5–8), and assume that the layered plates are monolithic with a single equivalent thickness. Predictions with $C=0$ neglect radial target inertia and only include target strength. The predictions that include only strength and those with strength and radial inertia bracket the experimental data. Thus, the closed-form, cavity-expansion equations give a good first order estimate and display the dominant problem parameters.

Summary and Discussion

In this study, we present results from a large number of perforation experiments with 5083-H116 target plates struck by ogive-nose rod projectiles and 7.62 mm APM2

bullets. The 7.62-mm-diameter, 10.7 g, APM2 bullet consists of a brass jacket, lead filler, and a 5.25 g, ogive-nose, hard steel core. The brass and lead were stripped from the APM2 bullets by the targets, so we conducted experiments with both the APM2 bullets and only the hard steel cores. Targets were 20, 40, and 60-mm-thick, where the 40, and 60-mm-thick targets were made up of layered plates in contact with each other. Residual velocity versus striking velocity data showed that the brass jacket and lead filler had a relatively small effect on the perforation process. In addition, we compared the hard steel core, perforation data with a closed-form, cavity-expansion model and showed reasonable good agreement. These experimental results and perforation equations display clearly the dominant problem parameters.

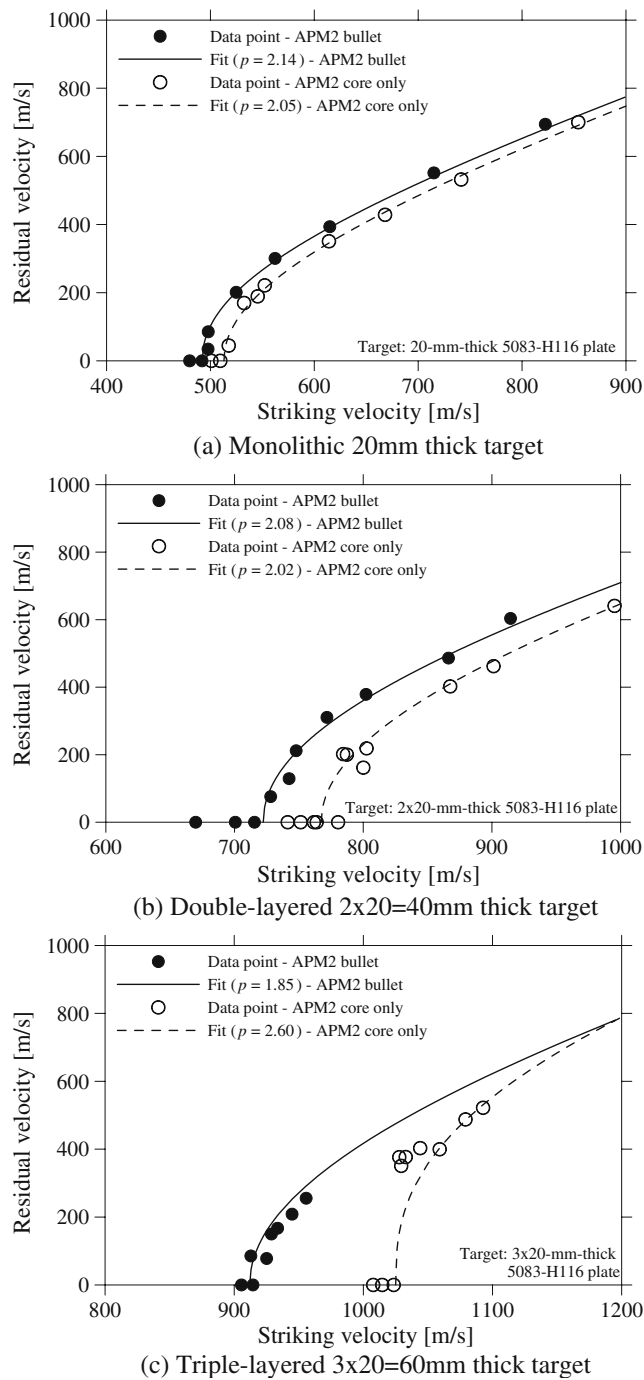


Fig. 10 Striking versus residual velocity curves for full APM2 bullets and hard cores only impacting a) single, b) double-layered and c) triple-layered AA5083-H116 target plates. (a) Monolithic 20 mm thick target, (b) Double-layered 2×20=40 mm thick target, (c) Triple-layered 3×20=60 mm thick target

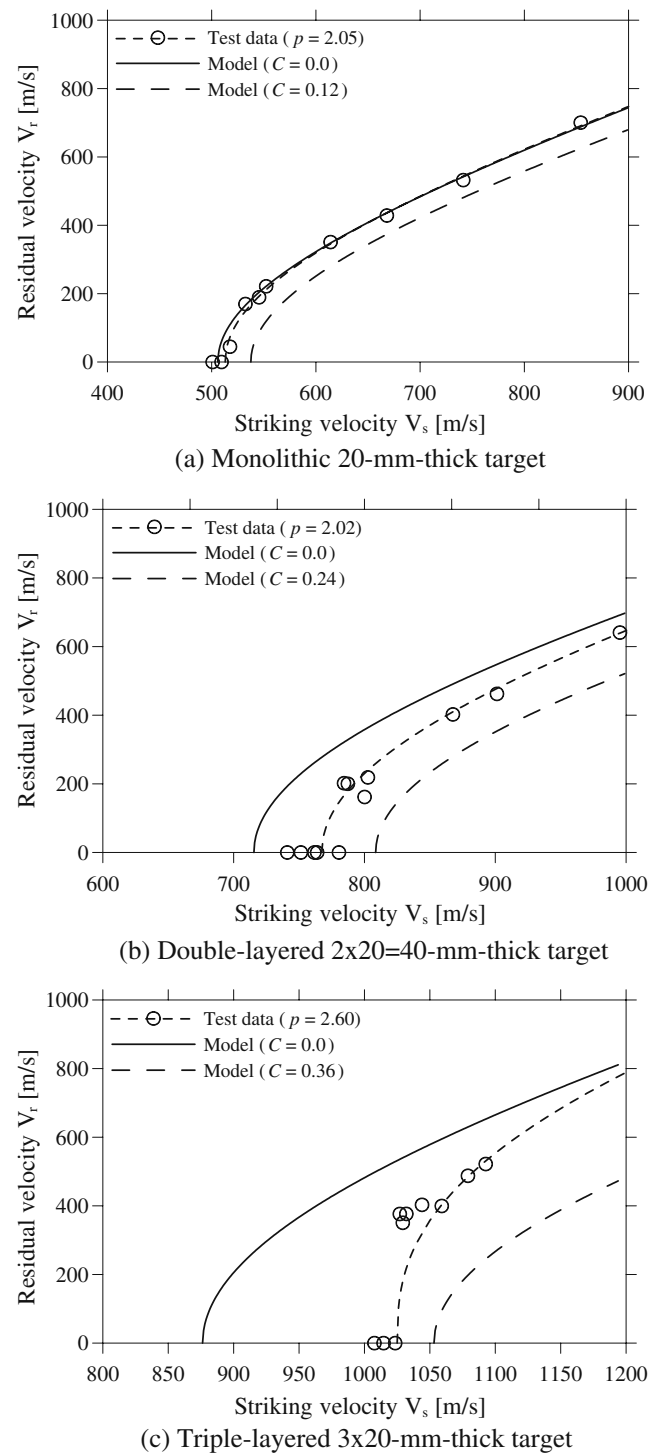


Fig. 11 Comparison of predicted and measured striking versus residual velocity curves for the hard core only of an APM2 bullet impacting a) single, b) double-layered and c) triple-layered AA5083-H116 target plates. (a) Monolithic 20-mm-thick target, (b) Double-layered 2×20=40-mm-thick target, (c) Triple-layered 3×20-mm-thick target

Acknowledgement The financial support of this work from the Structural Impact Laboratory (SIMLab), Centre for Research-based Innovation (CRI) at the Norwegian University of Science and Technology (NTNU), is gratefully acknowledged.

Appendix: Perforation Models

We give a full discussion of the cylindrical, cavity-expansion, perforation models in [1]. Briefly, the aluminum plate deformations are dominated by ductile hole-growth and the holes had nearly the diameter of the projectile shanks. To approximate ductile hole growth, the cylindrical, cavity-expansion method idealizes the target as thin independent layers that are compressed normal to the perforation direction. Thus, the analysis is simplified to one-dimensional motion in the radial plate dimension for an elastic-plastic material. We perform a cylindrically symmetric, cavity-expansion analysis, use these results to develop the perforation equations, and obtain closed-form perforation equations that predict the ballistic-limit and residual velocities.

A cylindrically symmetric cavity is expanded from zero initial radius at constant expansion velocity V . This expansion produces an elastic-plastic response. The elastic region has Young's modulus E and Poisson's ratio ν , and the plastic response region is taken as an incompressible, power-law hardening material. Data from uniaxial compression tests were curve fit with equations (2a,b) and results are shown in Fig. 2.

Our perforation models require the radial stress σ_r at the cavity surface versus cavity-expansion velocity V . From [1]

$$\sigma_r = \sigma_s + \rho_t B V^2 \quad (3a)$$

$$\sigma_s = \frac{Y}{\sqrt{3}} \left\{ 1 + \left[\frac{E}{\sqrt{3}Y} \right]^n \int_0^b \frac{(-\ln x)^n}{1-x} dx \right\}, \quad b = 1 - \gamma^2 \quad (3b)$$

$$B = \frac{1}{2} \left\{ \frac{1}{(1-\nu)\sqrt{1-\alpha^2}} \ln \left[\frac{1+\sqrt{1-\alpha^2}}{\alpha} \right] + \gamma^2 - 2 \ln[\gamma] - 1 \right\} \quad (3c)$$

$$\alpha^2 = \frac{\sqrt{3}(1-2\nu)}{2(1-\nu)} \left(\frac{\rho_t V^2}{Y} \right) \quad (3d)$$

$$\gamma^2 = \frac{2(1+\nu)Y}{\sqrt{3}E} \quad (3e)$$

where σ_s is the quasi-static radial stress required to open the cylindrical cavity and ρ_t is the target density. As discussed

in [16], the integral in equation (3b) is improper because of the integrand behavior near $x=0$. However, this singularity is integrable and the integral can be evaluated with an open formula such as the extended midpoint rule [17].

As discussed in [1], we accurately approximate equations (3c–e) with

$$\sigma_r = \sigma_s + \rho_t B_0 V^2 \quad (4)$$

where B_0 is a dimensionless constant obtained from curve-fitting equations (3c–e). The approximation given by equation (4) is required to obtain closed-form perforation equations because α and B_0 depend on V . Figure 6 shows the dimensionless radial stress at the cavity surface versus dimensionless cavity-expansion velocity from equations (3c–e) and equation (4) with $B_0=3.105$.

We now present closed-form perforation equations for rigid, ogive-nose projectiles that perforate aluminum target plates. For an ogive-nose projectile with striking velocity V_s , the ballistic-limit V_{bl} and residual velocity V_r are given by

$$V_{bl} = \left(\frac{2\sigma_s}{\rho_p} \frac{h}{(L+k_1l)} \right)^{1/2} \left[1 + C + \frac{2}{3}C^2 \right]^{1/2} \quad (5)$$

$$V_r = V_{bl} \left[\left(\frac{V_s}{V_{bl}} \right)^2 - 1 \right]^{1/2} \left[1 - C + \frac{1}{2}C^2 \right]^{1/2} \quad (6)$$

$$C = \frac{h}{(L+k_1l)} \frac{\rho_t}{\rho_p} B_0 N(\psi) \quad (7)$$

$$N(\psi) = 8\psi^2 \ln \left(\frac{2\psi}{2\psi-1} \right) - (1+4\psi) \quad (8)$$

In equations (5–8), the ogive-nose rod projectile has density ρ_p , shank length L , nose length l , diameter $2a$, caliber-radius-head ψ , and k_1 is given by equation (1b). The target plate has density ρ_t , thickness h , σ_s is given by equation (3b), and B_0 is given by equation (4).

As explained in [1], the terms in C in equations (5) and (6) come from a power-series expansion that is truncated after three terms. For the applications in [1] and this study, C is small enough that the next terms are negligible. For some applications [1], the value of C is very small compared to unity and equation (6) for residual reduces to

$$V_r = V_{bl} \left[\left(\frac{V_s}{V_{bl}} \right)^2 - 1 \right]^{1/2} \quad (9)$$

Based on the conservation laws and some assumptions, Recht and Ipsen [18] published equation (9) as an analytical model. They then determined V_{bl} experimentally and found

that equation (9) could accurately predict V_r for many data sets. Later, Lambert and Jonas [19, 20] observed that a modification of equation (9) provided a better fit to some experimental data. The Lambert-Jonas empirical equation is given by

$$V_r = (V_s^p - V_{bl}^p)^{1/p} \quad (10)$$

where p is the empirical constant used to best fit the data with the least squares method. Equation (10) reduces to equation (9) for $p=2$. In this study and a previous study [6], we use equation (10) to curve-fit the residual velocity versus striking velocity data.

References

- Forrestal MJ, Warren TL (2009) Perforation equations for conical and ogival nose rigid projectiles into aluminum target plates. *Int J Impact Eng* 36:220–225
- Børvik T, Forrestal MJ, Hopperstad OS, Warren TL, Langseth M (2009) Perforation of AA5083–H116 aluminum plates with conical-nose steel projectiles—calculations. *Int J Impact Eng* 36:426–437
- Dey S, Børvik T, Teng X, Wierzbicki T, Hopperstad OS (2007) On the ballistic resistance of double-layered steel plates: an experimental and numerical investigation. *Int J Solids Struct* 44:6701–6723
- Gooch WA, Burkins MS, Squillacioti RJ (2007) Ballistic testing of commercial aluminum alloys and alternative processing techniques to increase the availability of aluminum armor. *Proceedings of the 23rd International Symposium on Ballistics, Spain*, pp 981–988
- Anderson CE, Burkins MS, Walker JD, Gooch WA (2005) Time-resolved penetration of B₄C tiles by the APM2 bullet. *Comp Mod Eng Sci* 8(2):91–104
- Børvik T, Dey S, Clausen AH (2009) Perforation resistance of five different high-strength steel plates subjected to small-arms projectiles. *Int J Impact Eng* 36:948–964
- Børvik T, Hopperstad OS, Berstad T, Langseth M (2001) A computational model of viscoplasticity and ductile damage for impact and penetration. *European Journal of Mechanics – A/Solids* 20:685–712
- Børvik T, Hopperstad OS, Langseth M, Malo KA (2003) Effect of target thickness in blunt projectile penetration of Weldox 460 E steel plates. *International Journal of Impact Engineering* 28:413–464
- Dowling NE (1998) *Mechanical behavior of materials*. Second Edition, Prentice Hall, Upper Saddle River, NJ 07458: 64–65.
- Clausen AH, Børvik T, Hopperstad OS, Benallal A (2004) Flow and fracture characteristics of aluminum alloy AA5083–H116 as function of strain rate, temperature and triaxiality. *Materials Science and Engineering A* 365:260–272
- Benallal A, Berstad T, Børvik T, Clausen AH, Hopperstad OS (2006) Dynamic strain aging and related instabilities: experimental, theoretical and numerical aspects. *European Journal of Mechanics – A/Solid* 25:397–424
- US Army Research Laboratory (2007) Military Specifications MIL-DTL-46027 K (MR). Armor plate, aluminum alloy, weldability 5083, 5456, and 5059. AMSRL-WM-MA, US Army Research Laboratory, issued 31 July 2007.
- ASM International (1990) *Metals handbook*, tenth edition, Vol. 2 Properties and Selection: Non Ferrous Alloys and Special-Purpose Materials, Table 8.
- Kawahara W (1986) Compression materials testing at low to medium strain rates. Paper no. 86-WA-Mats-15, presented at the ASME Winter Annual Meeting, Anaheim, CA.
- Chen W, Skube S (2009) An experimental technique to obtain large strain compression data. Work in progress.
- Forrestal MJ, Romero LA (2007) Comment on “Perforation of aluminum plates with ogive-nose steel rods at normal and oblique impacts.” *Int J Impact Eng* 34:1962–1964
- Press WH, Flannery BP, Teukolsky SA, Vetterling WT (1990) *Numerical recipes*. Cambridge University Press, NY
- Recht RF, Ipsen TW (1963) Ballistic perforation dynamics. *ASME J Appl Mech* 30:384–390
- Lambert JP, Jonas GH (1976) Towards standardization in terminal ballistic testing: velocity representation. *Ballistic Research Laboratories, Report BRL-R-1852*, USA.
- Zukas JA (1990) *High velocity impact dynamics*. Wiley, New York, pp 424–427